This article has been accepted for inclusion in a future issue of this journal. Content is final as presented, with the exception of pagination.

Inchworm Inspired Multimodal Soft Robots With Crawling, Climbing, and Transitioning Locomotion

Yifan Zhang, Dezhi Yang, Peinan Yan, Peiwei Zhou, Jiang Zou, and Guoying Gu, *Senior Member, IEEE*

***Abstract*—Although many soft robots, capable of crawling or climbing, have been well developed, integrating multimodal locomotion into a soft robot for transitioning between crawling and climbing still remains elusive. In this work, we present a class of inchworm-inspired multimodal soft crawling-climbing robots (SCCRs) that can achieve crawling, climbing, and transitioning between horizontal and vertical planes. Inspired by the inchworm's multimodal locomotion, which depends on the "Ω" deformation of the body and controllable friction force of feet, we develop the SCCR by 1) three pneumatic artificial muscles based body designed to produce "Ω" deformation; 2) two negative pressure suckers adopted to generate controllable friction forces. Then a simplified kinematic model is developed to characterize the kinematic features of the SCCRs. Lastly, a control strategy is proposed to synchronously control the "Ω" deformation and sucker friction forces for multimodal locomotion. The experimental results demonstrate that the SCCR can move at a maximum speed of 21 mm/s (0.11 body length/s) on horizontal planes and 15 mm/s (0.079 body length/s) on vertical walls. Furthermore, the SCCR can work in confined spaces, carry a payload of 500 g (about 15 times the self-weight) on horizontal planes or 20 g on vertical walls, and move in aquatic environments.**

***Index Terms*—Inchworm inspired, locomotion transition, multimodal locomotion, soft climbing robot.**

I. Introduction

MULTIMODAL locomotion, including crawling and climbing, is widely observed in various species (such as caterpillars, snakes, cats, etc.) and brings the animals with strong environmental adaptability. During the past decades, numerous bio-inspired crawling or climbing robots have been invented for various applications like maintenance, surveillance, and cleaning. Besides, researchers have succeeded in creating robots with the transitioning function between crawling and climbing to enlarge their workspace and help them move in complex environments. The concept of transitioning was first realized by robots using mechanisms like leg, wheel, propeller, etc. [1]–[3]. Recently, several robots that are composed of flexible multilinks and innovative adhesion pads are developed with the transitioning function [4]–[6]. However, most of these robots are composed of rigid actuation components and complex structures. As a result, they generally suffer from heavy body weight and lack of self-adaptability in unstructured environments, which is fundamentally different from the biological animals.

The advancement in soft materials and artificial muscles (such as pneumatic elastomer actuators [7], [8], dielectric elastomer actuators [9], [10], shape memory materials [11]–[13], etc.) enables researchers to design soft crawling or climbing robots with bio-inspired structures and functions. Compared with their rigid counterparts, soft robots generally have the advantages of simple structures, light weight, safe operation, low price, and high self-adaptability [14]–[18].

For soft robot design, crawling locomotion is one of the most prevalent gaits due to its simple working principle and easiness to employ [19]–[21]. For instance, Rafsanjani *et al.* [22] covered a snake-skin inspired soft robot that is composed of fiber-reinforced elastomer elongation actuators and kirigami skin. The directional frictional properties of the functional skin enable the robot to crawl efficiently. Ge *et al.* [23] developed an earthworm inspired soft crawling robot, which replicates the peristaltic wave and retractable setae (bristles) mechanism of the animal. Also, inspired by inchworms, many soft crawling robots have been well developed [24]–[28]. In general, soft crawling robots consist of one or more bending or elongation actuators that can generate periodical actuation. Various structures using mechanisms like friction, electroadhesion, gecko adhesion, claws, etc., are adopted to transmit the periodical actuation into directional crawling.

Similar to crawling, the climbing locomotion shares the same gait but is more challenging because it needs to overcome gravity. For instance, Gu *et al.* [29] presented the very early wall-climbing soft robot, which is composed of dielectric-elastomer artificial muscles and electro-adhesive foot pads. The robot can also accomplish the crawling locomotion with similar gaits. Zang *et al.* [30] demonstrated a snake-inspired rod-climbing soft robot using winding locomotion, which can climb and turn along the rods of different sizes carrying a payload of 500 g (25+ times self-weight). Alternatively, by introducing the 3D printing and modular design approach, Xie *et al.* [31] developed a kind of

Manuscript received May 30, 2021; revised September 2, 2021; accepted September 18, 2021. This work was supported in part by the National Natural Science Foundation of China under Grant 52025057 and Grant 91848204 and in part by the Science and Technology Commission of Shanghai Municipality under Grant 20550712100. This paper was recommended for publication by Associate Editor W. He and Editor A. Menciassi upon evaluation of the reviewers' comments. *(Yifan Zhang and Dezhi Yang are co-first authors.) (Corresponding author: Guoying Gu.)*

The authors are with the Robotics Institute, School of Mechanical Engineering, Shanghai Jiao Tong University, Shanghai 200240, China, and also with the State Key Laboratory of Mechanical System and Vibration, Shanghai Jiao Tong University, Shanghai 200240, China (e-mail: franklin369@sjtu.edu.cn; powertower@sjtu.edu.cn; peinanyan@sjtu.edu.cn; 1549224905@sjtu.edu.cn; zoujiang@sjtu.edu.cn; guguoying@sjtu.edu.cn).

This article has supplementary material provided by the authors and color versions of one or more figures available at https://doi.org/10.1109/TRO.2021.3115257.

Digital Object Identifier 10.1109/TRO.2021.3115257

This article has been accepted for inclusion in a future issue of this journal. Content is final as presented, with the exception of pagination.

inchworm-inspired robot, which can climb in pipes with various inclinations ranging from 0° to 90°.

Although many soft crawling or climbing robots have been reported in previous work, to the best of our knowledge, none of them can simultaneously achieve the transition between crawling and climbing locomotion. The main challenges of developing soft robots with transitioning locomotion depend on the following two facts. First, for transitioning locomotion, the soft robot needs to perform multidegree of freedom (DOF) deformation so that it can lift one of its feet away from the ground and reach for a foothold spot on the wall. The process requires enough actuation forces that can lift part of the robot's self-weight. Second, soft actuators suffer from buckling effects in some configurations due to their low material stiffness and infinite motion DOFs. We need to design the control strategies to avoid the buckling effects and keep the robot stable in every configuration.

In this work, we present a multimodal soft crawling-climbing robot (SCCR). Inspired by inchworms, which can achieve multimodal locomotion through synchronously controlling the body's deformation and feet's friction forces, we develop our SCCR by connecting three bending fiber-reinforced pneumatic artificial muscles (PAMs) in series to mimic the "Ω" deformation of the inchworm. Besides, two negative pressure sucker feet are applied to generate controllable friction forces. To build and verify the design, we develop a simplified kinematic model to evaluate the workspace of the body of our SCCR. Furthermore, we propose a synchronous control strategy for the SCCR to achieve multimodal locomotion gaits by controlling the PAMs' quasi-static deformation shapes and suckers anchoring status. We also conduct several experiments to characterize the multimodal locomotion performances. The experimental results demonstrate that the SCCR moves at the highest speed of 21 mm/s (0.11 body length/s) and is capable of dragging a payload of 500 g (about 15 times the self-weight) on plastic horizontal planes. The SCCR can also climb on a vertical wall at the speed of 15 mm/s (0.079 body length/s) and carry a payload of 20 g. Actuated by water, the SCCR can even accomplish different locomotion in aquatic environments.

Compared with our previous conference paper [32], which proposed a soft robot that can accomplish transitioning locomotion from a horizontal plane to a 75° slope, the main improvements and contributions of this work are as follows.

1) We increase the robot body control DOFs from two to three. By dividing the head-abdomen actuator into head and abdomen PAMs, the added PAM helps enlarge the robot workspace, makes the deformation of the robot symmetric, and enables full control of robot head position and posture. Thus, in complicated mechanical environments, a combination of PAMs can provide multidirectional forces to confront the peel-off effect of the robot self-weight and help the robot climb flexibly on vertical walls.

2) An analytical model is developed to evaluate the bending behaviors of PAMs under different input pressures. With the derived pressure-deformation relationship, we can accomplish real-time open-loop synchronous pressure control of PAMs' bending deformation and the anchoring states of suckers via a multichannel air pressure control system.

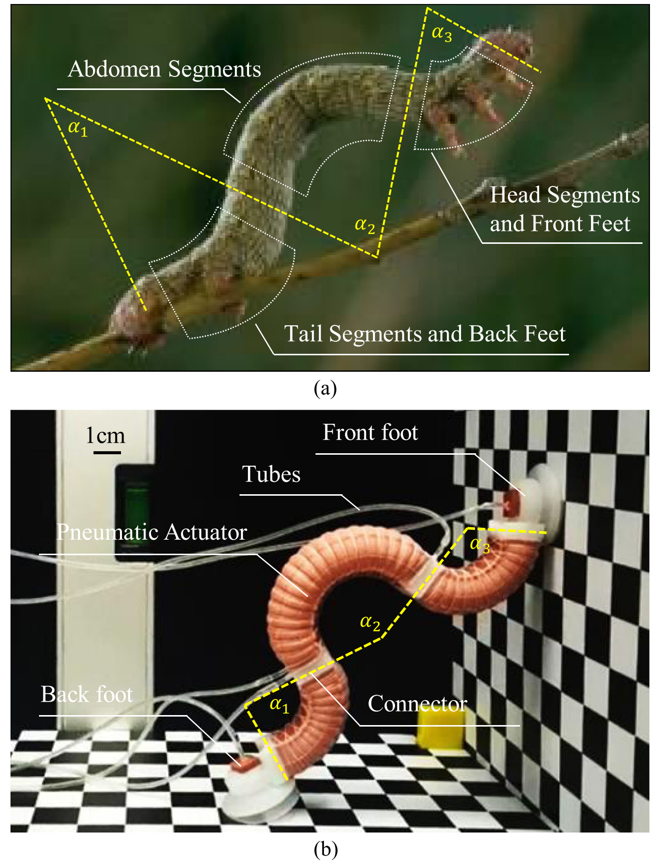

Fig. 1. Comparison between the biological inchworm and the robot inchworm. (a) Simple division of inchworm's body parts. Thirteen body segments are divided into three groups (head, abdomen, and tail) according to "Ω" deformation of the inchworm body. (b) SCCR transitions between crawling and climbing locomotion.

3) To characterize the robot locomotion gaits, a simplified kinematic model is introduced to evaluate the workspace of the SCCR. Based on the model, we are able to calculate the relative positions of two robot feet in different robot joint configurations. Hence, we can design the feet transitioning paths, step length, and locomotion directions according to the environmental constraints.

II. Robot Design

A. Bioinspired Actuator Design

Inspired by the "Ω" deformation of inchworm body, we design the structure and arrangement of PAMs. In crawling and climbing locomotion of biological inchworms, we observe that the inchworm bends or stretches its body segments simultaneously and the inchworm body contracts periodically into an "Ω" shape [33]–[35]. When the inchworm comes across an obstacle or transitions between crawling and climbing, it can control the bending angles of body segments respectively to explore with its head for suitable foothold spots. Despite the fact that the front and back feet land in different spots, the contracted inchworm body can be regarded as a mutation of "Ω" shape [Fig. 1(a)].

This article has been accepted for inclusion in a future issue of this journal. Content is final as presented, with the exception of pagination.

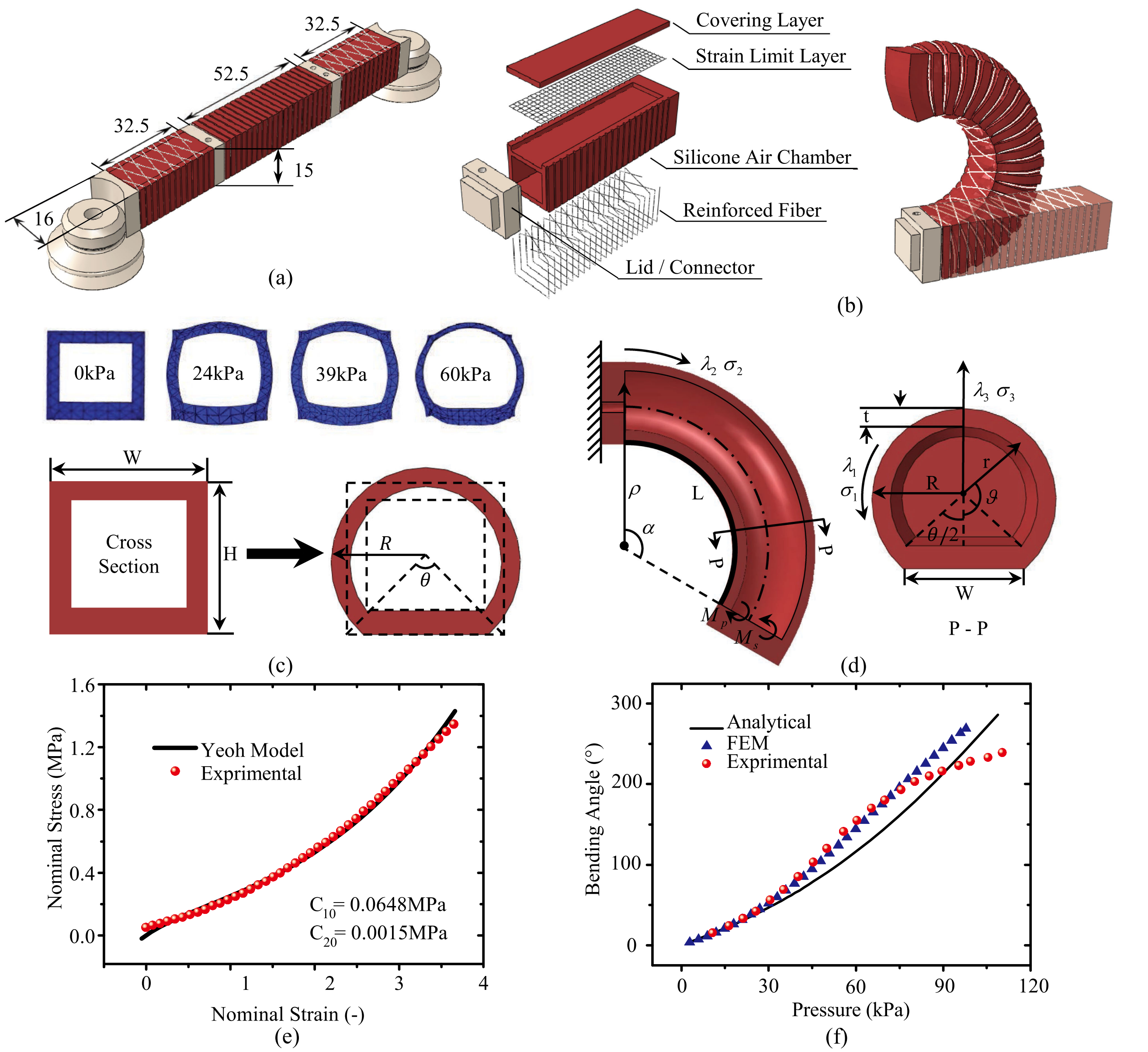

Fig. 2. Design and modeling of fiber-reinforced PAMs with strain limit layers. (a) Dimensions of the assembled SCCRs. The length of three PAMs are 32.5, 52.5, and 32.5 mm, respectively. (b) Structure of fiber-reinforced PAMs, each of which consists of a covering layer of silicone, a strain limit layer, a silicone air chamber, reinforcement fibers, and lids/connectors. (c) Evolution of the PAM cross section from 0 to 60 kPa measured with FEM simulation. The approximation of actual cross section can be decomposed into a curve and a straight line. (d) Parameters used to describe the theoretical bending deformation and stresses along three directions. (e) Strain–stress experiment data and Yeoh model fitting results of mixed silicone material M4601:Ecoflex 0030 = 1:1 (by weight). The Yeoh model is used for FEM simulation. (f) Comparison of the FEM simulation, experiment results, and analytical model.

The inchworm body segments display limited elongation abilities but strong bending abilities. Some body segment can even provide a bending deformation of over 15°. In most observed locomotion, the bending direction (upward or downward convexly) for each body segment keeps unchanged. More specifically, the head segment group (first five segments, counted from head) and the tail segment group (from the tenth to the thirteenth segment, counted from head) generally bends downward convexly, while the abdomen segment group (from the sixth to the ninth segment, counted from head) generally bend upward convexly.

The division of the inchworm body inspires us to replicate the bending function of different segment groups using head, abdomen, and tail PAMs [Fig. 1(b)]. Each PAM is composed of a silicone covering layer, a strain limit layer, a silicon air chamber, reinforce fibers, and sealing lids/connectors [Fig. 2(b)]. The cross section of each PAM is rectangular. When inflated with air or water, the silicone air chambers expand like balloons. While the reinforce fibers, which are winded evenly along the four surfaces of PAMs, constrain the radial expansion and enhance the axial elongation of the air chambers. In order to produce the bending deformation, nonstretchable strain limit layer is embedded in one side of the air chamber and restrains the stretch of part of the PAM and causes the bending deformation. For the fabricated SCCR shown in Fig. 2(a), we set the strain limit layers on the top surface of the head/tail PAM and on the bottom surface of the abdomen PAM. This arrangement results in the desired bending directions of three PAMs.

B. PAM Analytical Modeling

We build an analytical model to calculate the relationship between PAM bending angles and input air pressures under constant curvature assumption [28], [36], [37] based on which we can obtain the required actuation pressures for any robot configuration. The finite-element method (FEM) results in Fig. 2(c) show that the cross section of the PAM develops from a rectangle (deflated, 0 kPa) to an approximate circle (inflated, 60 kPa) and barely changes after that. It is observed that the fiber reinforcement cannot completely constrain the shape change of the air chamber outer bound, while the nonstretchable strain limit layer restrains the lower side of the cross section much better. Thus, in the analytical model, we assume that the PAM cross-sectional shape is made up of a straight line (strain limit layer) and part of a circle (PAM-free chamber walls) and keeps unchanged during the whole bending deformation process. The curve length equals the total length of three free sides of actual rectangular cross section and the straight line measures the width of strain limit layer. This assumed cross-sectional shape shares fewer similarities with the actual cross section under low pressure while it can better describe the actual inflated cross section under high pressure. This simplification takes the cross-sectional shape evolution into consideration and keeps a reasonable calculation complexity and accuracy.

Specifically, we consider a PAM with an original outer rectangular cross section of the width W and height H [Fig. 2(c)]. The assumed cross section is composed of a curve that measures $W + 2H$ and a straight line that measures W. The radius R of the curve and corresponding central angle θ of the strain limit layer can be calculated by

$$(2\pi - \theta)R = W + 2H \tag{1}$$

$$\theta = 2\arcsin(W/2R). \tag{2}$$

On each cross section [Fig. 2(d)], the actuation torque M_P of the input air pressure P_{in} against the bottom strain limit layer can be calculated as

$$M_P = \frac{1}{6}P_{\text{in}}\left[3t_0 + (R - t_0)\cos\frac{\theta}{2}\right](R - t_0)^2 \sin\theta + \int_0^{R-t_0}\int_{\frac{\theta}{2}}^{2\pi-\frac{\theta}{2}} P_{\text{in}} r\left(R\cos\frac{\theta}{2} - r\cos\vartheta\right) d\vartheta dr \tag{3}$$

where the first term represents the actuation torque performed by the pressure in a triangle area formed by the inner wall of strain limit layer side and the curve center. The integral term represents the actuation torque performed by the pressure in the remaining sector area.

The relationship between stress and strain is determined by the material properties. We suppose that the material is incompressible and isotropic. The Neo-Hookean model is applied to express the deformation behavior of the mixed silicone material [38]. The strain energy density function is

$$E = C(I_1 - 3) \tag{4}$$

where the material constant $C = 53$ kPa is identified based on the strain–stress experiment results and I_1 is the first invariant of three principal stretch ratios λ_1 (circumferential direction), λ_2 (axial direction), and λ_3 (radial direction)

$$I_1 = \lambda_1^2 + \lambda_2^2 + \lambda_3^2. \tag{5}$$

Then the corresponding principal stress can be derived as

$$\sigma_i = \lambda_i \frac{\partial E}{\partial \lambda_i} - p. \tag{6}$$

Due to the constraint of reinforce fibers, the strain in circumferential direction and the stress in radial direction can be ignored, which means $\lambda_1 = 1$ and $\sigma_3 = 0$. The principle stresses are

$$\sigma_1 = \lambda_1 \frac{\partial E}{\partial \lambda_1} - p = 2C\lambda_1^2 - p = 2C(1 - \lambda_3^2) \tag{7}$$

$$\sigma_2 = \lambda_2 \frac{\partial E}{\partial \lambda_2} - p = 2C\lambda_2^2 - p = 2C(\lambda_2^2 - \lambda_3^2) \tag{8}$$

$$\sigma_3 = \lambda_3 \frac{\partial E}{\partial \lambda_3} - p = 2C\lambda_3^2 - p = 0 \tag{9}$$

$$p = 2C\lambda_3^2. \tag{10}$$

Incompressible material model [39] requires

$$\lambda_1\lambda_2\lambda_3 = 1. \tag{11}$$

Combining (10) with (11) and (13), we can derive

$$\sigma_2 = 2C\left(\lambda_2^2 - \frac{1}{\lambda_2^2}\right). \tag{12}$$

The stretch of the air chamber materials produces a restoring torque M_S, which can be expressed as

$$M_S = \int_0^W \int_0^{t_0\lambda_3} \sigma_2 y dy dx + \int_{\frac{\theta}{2}}^{2\pi-\frac{\theta}{2}} \int_{R-t_0\lambda_3}^{R} \sigma_2 r\left(R\cos\frac{\theta}{2} - r\cos\vartheta\right) dr d\vartheta. \tag{13}$$

On each cross section, M_S is the torque imposed by axial stress of the materials [Fig. 2(d)]. The first integral term represents the torque proposed by the material restoring force on strain limit layer side and the second term represents the torque proposed by the restoring force in free side materials. For simplification, we suppose that the principal axial stretch ratio λ_2 keeps unchanged along the radial direction. By substituting σ_2 into (13), M_S can be expressed as

TABLE I
PARAMETER TABLE FOR ANALYTICAL MODEL IN FIG. 2(F)

Parameter	L/mm	W/mm	H/mm	R/mm	t_0/mm	$\theta/°$
Value	50	16	15	10.24	2	103

$$M_S = \int_0^{t_0\lambda_3} 2CW\left(\lambda_2^2 - \frac{1}{\lambda_2^2}\right) y dy + \int_{\frac{\theta}{2}}^{2\pi-\frac{\theta}{2}} \int_{R-t_0\lambda_3}^{R} 2C\left(\lambda_2^2 - \frac{1}{\lambda_2^2}\right)\left(R\cos\frac{\theta}{2} - r\cos\vartheta\right) r dr d\vartheta. \quad (14)$$

Under quasi-static conditions, M_S reaches an equilibrium with M_P

$$M_S = M_P. \quad (15)$$

As is shown in Fig. 2(d), we suppose that the PAM shares an original length L, a bending angle α, and a bending radius ρ in deformed configuration, and then we obtain the axial stretch ratio λ_2 at any position (ϑ, r)

$$L = \alpha\rho \quad (16)$$

$$\lambda_2(\vartheta, r) = 1 + \frac{1}{\rho}\left(R\cos\frac{\theta}{2} - r\cos\vartheta\right). \quad (17)$$

By substituting (16) and (17) into (15), we can cancel the variables λ_2 and ρ and then calculate the relation between input pressure P_{in} and the bending angle α. Since M_S is the integral over the bending angle α and P_{in} can be extracted from the integral of M_P, we can calculate the required P_{in} for any desired bending angle α. To evaluate the analytical model, we conduct the numerical FEM simulation based on the strain–stress experiment results shown in Fig. 2(e). The experiment results and the analytical model results are compared in Fig. 2(f), and the specific parameters for calculating the analytical model results are listed in Table I. The 50 mm PAM can perform a bending deformation of over 200° with an actuation pressure of 100 kPa. The FEM results agree with the experiments for pressure range of 0–80 kPa. For the analytical model, two factors may explain the errors. One is the constant curvature assumption and the simplification of the PAM cross section. The other is the nonlinear behavior of the materials in large deformation.

C. Robot Workspace

When one end of the SCCR is anchored to the ground, we can obtain the other end's position and posture according to the bending angles of three PAMs. As shown in Fig. 3(a), we simplify and represent the "geometric inchworm" using three rectangular shapes with constant bending curvatures. We denote that the lengths of tail, abdomen, and head PAMs are L_1, L_2, and L_3, respectively, and the corresponding PAM bending angles are α_1, α_2, and α_3, respectively. By introducing five coordinates and filling in the D-H parameter table (Table II), we can obtain the posture (x, y, ϕ) of the terminal joint. The transition matrix from

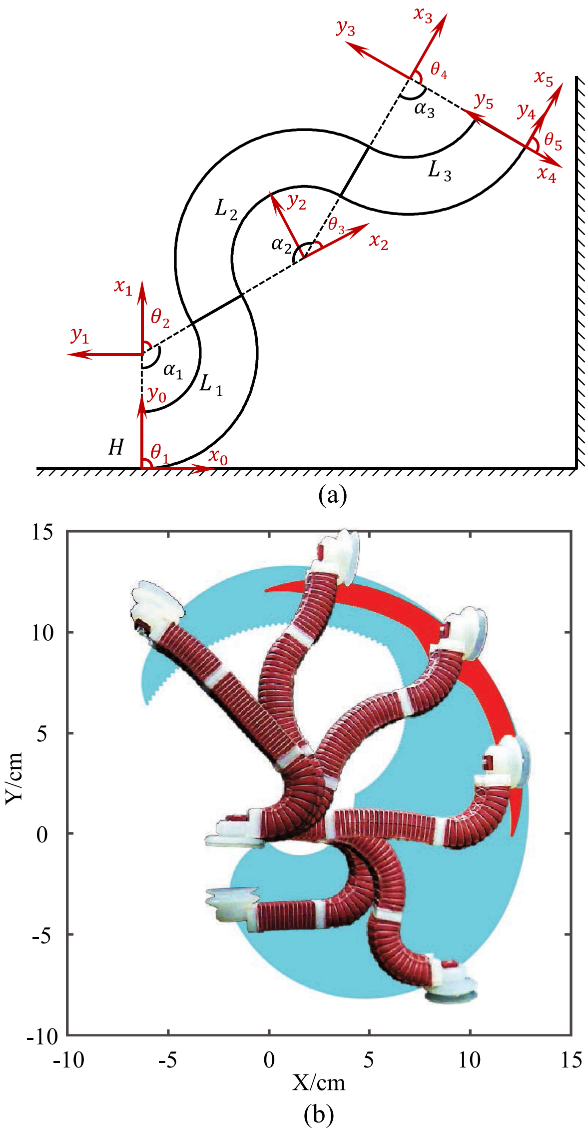

Fig. 3. Kinematic model of the SCCR. (a) Geometric simplification of the SCCR deformed shape with three bent rectangles. The posture of robot head (x, y, ϕ) can be obtained through coordinates 1–5 when the other end of the SCCR is fixed on the ground. (b) Workspace of the SCCR terminal joint when one end is fixed on the ground. The blue shape illustrates the reachable workspace of the SCCR head. The red shape represents the workspace of the SCCR head with the constraint $\phi = \alpha_1 - \alpha_2 + \alpha_3 = \pi/2$.

TABLE II
D-H PARAMETERS TABLE FOR JOINTS 1–5

Link #	a_i	θ_i
1	$L_1/\alpha_1 + H$	$\pi/2$
2	$L_1/\alpha_1 + L_2/\alpha_2 + H$	$-\pi + \alpha_1$
3	$L_2/\alpha_2 + L_3/\alpha_3 + H$	$\pi - \alpha_2$
4	$L_3/\alpha_3 + H$	$-\pi + \alpha_3$
5	0	$\pi/2$

coordinate i to $i+1$ is expressed as

$$T_i^{i-1}(\theta_i) = \begin{bmatrix} \cos\theta_i & -\sin\theta_i & a_i\cos\theta_i \\ \sin\theta_i & \cos\theta_i & a_i\sin\theta_i \\ 0 & 0 & 1 \end{bmatrix}. \quad (18)$$

The position of the terminal joint (x, y) in the base coordinate (with respect to the anchored tail) can be calculated from its position in its own coordinate (x_e, y_e) and the total transition matrix $T_e^b(q)$ as

$$\begin{bmatrix} x \\ y \\ 1 \end{bmatrix} = T_e^b(q) \begin{bmatrix} x_e \\ y_e \\ 1 \end{bmatrix} = \prod_{i=0}^{4} T_{i+1}^{i}(\theta_{i+1}) \begin{bmatrix} 0 \\ 0 \\ 1 \end{bmatrix}. \quad (19)$$

The posture ϕ of the terminal joint can be expressed as

$$\phi = \alpha_1 - \alpha_2 + \alpha_3. \quad (20)$$

The two-dimensional workspace can be calculated when two more constraints are included for PAM deformation: 1) the stretch of the materials does not exceed the elastic limit; 2) different parts of the SCCR body do not conflict with each other. A larger workspace will enable the SCCR to transition more flexibly between different locomotion and provide more route planning choices when finishing different tasks. Due to the complex expression of the workspace with different constraints (like self-collision, material deformation limits, etc.), we adopt a numerical method to find that the largest workspace area [Fig. 3(b)] is obtained around the PAM length ratio 32.5 mm (tail): 52.5 mm (abdomen): 32.5 mm (head). The red shape represents the reachable area where the terminal joint posture follows $\phi = \alpha_1 - \alpha_2 + \alpha_3 = \pi/2$. With the cooperation of three PAMs, the SCCR can lift its head to the height of 12 cm. Fixing the back foot at the origin point, the SCCR head can also reach some positions in the second and fourth quadrants.

D. Characterization of Sucker Feet

Considering the adhesion force required in payload carrying tasks, initiative raising of robot self-weight, and other applications, we adopt double-layer silicone suckers as the adhesive foot pads. The alternative anchoring and releasing of sucker pads, cooperating with the "Ω" deformation of body, enable the SCCR to finish different gaits. The three-dimensional sketch and main parameters of the sucker are illustrated in Fig. 4(a). The sucker has a bellow buffer layer so that the bottom hemline can easily form a seamless seal with the surface. After air is pumped out from the sucker, the bellow buffer layer is compressed to improve sucker's total stiffness and provides resistance to external force and torque [Fig. 4(a)]. We characterize the normal and tangent anchoring forces of silicone suckers against the applied negative pressure. The measurement results of sucker adhesion forces on plastic, wood, and paper surfaces are shown in Fig. 4(b). In free state (0 kPa), the friction force between sucker feet and the ground measures approximately 0.1–0.2 N. Whereas, the sucker tangent anchoring force is above 10 N under −40 kPa or higher negative pressure, which is enough to help lift the robot self-weight in climbing locomotion. Based on the results in Fig. 4(b), we can adjust the friction forces of the sucker feet by controlling the pressure of each foot.

When moving on the ground, the SCCR periodically drags or pushes one of the sucker feet by contracting or stretching the robot body. The body blocking force is measured against

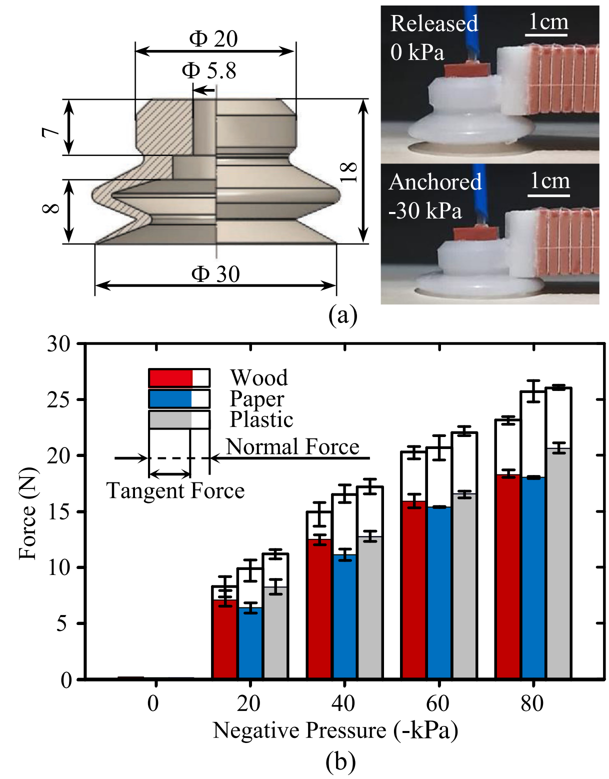

Fig. 4. Characterization of double-layer silicone sucker feet. (a) Three-dimensional sketch and main parameters of the sucker. Sucker releasing (0 kPa) and anchoring (–30 kPa) status on a horizontal wooden plane. (b) Sucker normal and tangent anchoring force are measured on wood, paper, and plastic planes under different air pressures. The filled bar height represents the tangent anchoring force and the blank bar height represents the corresponding normal anchoring force.

the displacement when the robot deforms into different configurations. The experimental results are illustrated in Fig. 5(b), which demonstrate that the blocking force ranges between 0.2 (free state friction force) and 10 N (anchoring state tangent adhesion force). Furthermore, larger tangent anchoring force for the anchored foot, compared with the blocking force, guarantees that the foot anchoring status will hardly be impacted by the movement of the SCCR.

E. Gait Design for Different Locomotion

Inspired by the study on inchworm locomotion [33]–[35], we provide the geometric gait design for the SCCR in crawling, climbing, and transitioning locomotion in this section. Each locomotion is first divided into several stages and we design the body configuration and feet anchoring strategies for each stage based on the inspiration of biological inchworms.

For crawling and climbing, the two ends of the SCCR always move in the same plane; thus, the terminal joint posture follows the constraint $\phi = \alpha_1 - \alpha_2 + \alpha_3 = 0$ in all different stages. According to the total transition matrix obtained in equation (19), we can determine the gait step length in these two locomotion by tuning the bending angles of three PAMs in different stages.

As shown in Fig. 6, the crawling locomotion can be further divided into two types: squirming and inching, which have

This article has been accepted for inclusion in a future issue of this journal. Content is final as presented, with the exception of pagination.

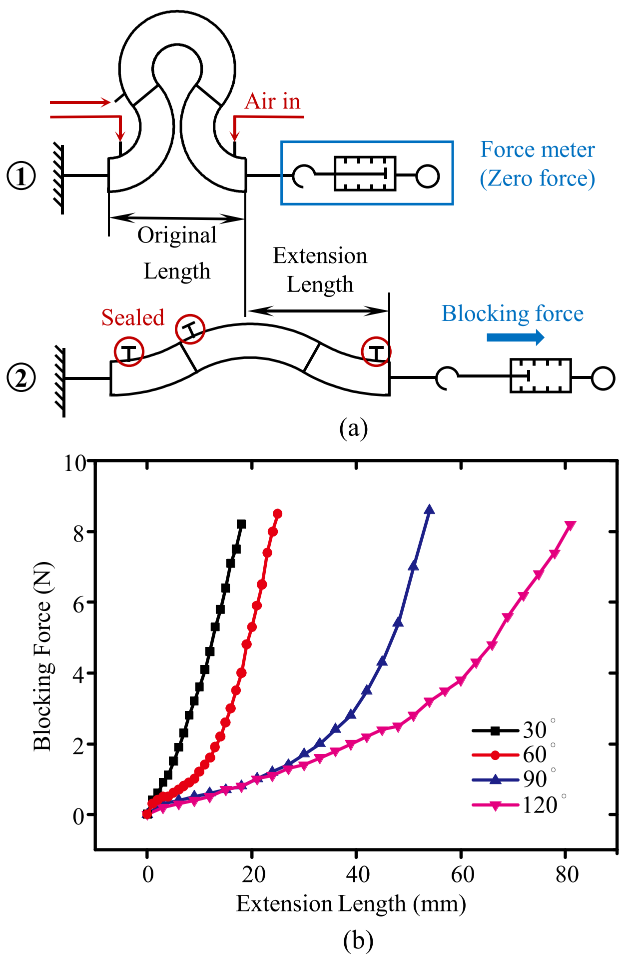

Fig. 5. (a) Schematic diagram of the body blocking force experiment. In step 1, three PAMs are pressurized and one end of the SCCR is fixed. In step 2, the PAMs are first sealed and one end of the SCCR is slowly pulled using a force meter. The blocking force is recorded with the extension length. (b) SCCR body blocking forces in different configurations when one end is anchored on the ground. Different lines represent the bending angles of head or tail PAM, and the bending angles of three PAMs follow the constraints: $\phi = \alpha_1 - \alpha_2 + \alpha_3 = 0$ and $\alpha_1 = \alpha_3$.

similar actuation sequence but different moving directions. Under the constraints of $\phi = \alpha_1 - \alpha_2 + \alpha_3 = 0$ and $\alpha_1 = \alpha_3$, the arched body length is first extended and then contracted as α_1 increases, while the body height keeps increasing as α_1 increases [Fig. 6(a)]. Depending on the arched body length, we define the crawling locomotion with a smaller arched body length (from point II to point III) in stages 2, 3, and 4 as inching-type [Fig. 7(a)] and the crawling locomotion with a larger arched body length than original (before point II) in stages 2, 3, and 4 as squirming-type [Fig. 7(b)]. With identical actuation sequence, the arched body pushes the front foot rightwards in stage 5 of inching-type crawling, while it pulls the front foot leftwards in stage 5 of squirming-type crawling, resulting in completely opposite moving directions. Theoretically, the arched body height of squirming-type crawling locomotion ranges from 15 (original body height) to 60 mm (body height at point II) depending on the selected step length. In inching-type crawling locomotion, the arched body height increases from 60 (body height at point II) to 80 mm (body height at point III) as the arched body length decreases.

The climbing gaits shown in Fig. 7(c) are similar in all six stages with the inching-type crawling locomotion. The PAM bending angles also follow $\phi = \alpha_1 - \alpha_2 + \alpha_3 = 0$. In stage 1, the front foot is anchored and the body is fully stretched. In stage 2, the SCCR contracts into an "Ω" shape to drag the back foot frontwards to shorten the distance between two feet. In stages 3 and 4, we switch the anchoring status for two sucker feet. The front foot is released after the back foot is anchored. In stage 5, the SCCR body stretches out to reach the foothold spot in the next step. In the last stage, both feet are anchored, after which we release the back foot to enter the new stage 1 of next gait cycle. According to the designed locomotion gaits as shown in Fig. 7(a)–(c), we can control the directional crawling and climbing locomotion of SCCRs by synchronously controlling the PAM deformation and sucker anchoring status in different stages.

For transitioning locomotion [Fig. 7(d)], we suppose that the SCCR starts moving from the configuration in crawling stage 4, which is regarded as the new stage 1. In stage 2, the SCCR lifts the front part of its body to get over the wall corner. In stages 3 and 4, the SCCR presses the front sucker against the vertical wall and then switches the anchoring status of two feet. In stage 5, the SCCR contracts into an "Ω" shape again to drag the back foot onto the wall. After the back foot is anchored again in stage 6, the SCCR can continue to move from stage 3 of climbing locomotion. In stages 3 and 4, the front foot is attached to the wall and the back foot is attached to the ground. In this case, the bending angles of the PAMs follow the constraint $\phi = \alpha_1 - \alpha_2 + \alpha_3 = \pi/2$.

III. Experiment Setups

A. Fabrication

The production of fiber-reinforced PAMs with strain limit layers has been introduced and discussed in the previous literature [36]. With the following five steps, we can fabricate the SCCR and connect it with the multichannel pressure control system.

1) Molding Air Chambers: An air chamber with a wall thickness of 2 mm is molded using mixture of two kinds of silicone gel, Elastosil M4601 (Wacker Chemie AG, Germany) : Ecoflex 0030 (Smooth-on Inc., PA, USA) = 1:1 by weight. The mixture of two silicone gels has desired viscosity in liquid status and hardness in solid status, which enables us to fabricate PAMs with thinner walls and less defection.

2) Burying Strain Limit Layers: The nonstretching strain limit layer is cut into appropriate rectangular shape (14 mm×32.5 mm or 14 mm×52.5 mm, based on the PAM type) and then buried into the reserved superficial grooves with the same silicone mixture. Each PAM has an outside cross section of 15 mm×16 mm, 2 mm total wall thickness on strain limit layer side and the other three free sides. The length of three PAMs are 32.5, 52.5, and 32.5 mm, respectively.

3) Winding Reinforce Fibers: We seal the air chamber with 3D printed connectors or lids and wind the reinforced fibers at

This article has been accepted for inclusion in a future issue of this journal. Content is final as presented, with the exception of pagination.

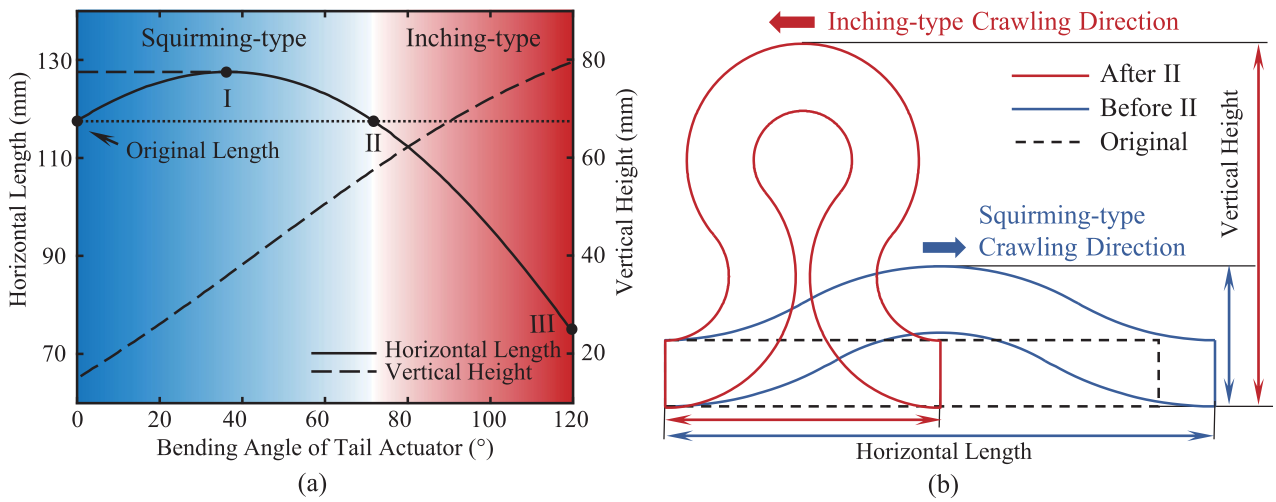

Fig. 6. SCCR body length and height for two types of crawling locomotion. (a) In crawling locomotion, the SCCR horizontal body length and vertical body height changes with the bending angles of the PAMs. (b) Crawling locomotion can be further divided into squirming-type and inching-type based on the moving direction and step length.

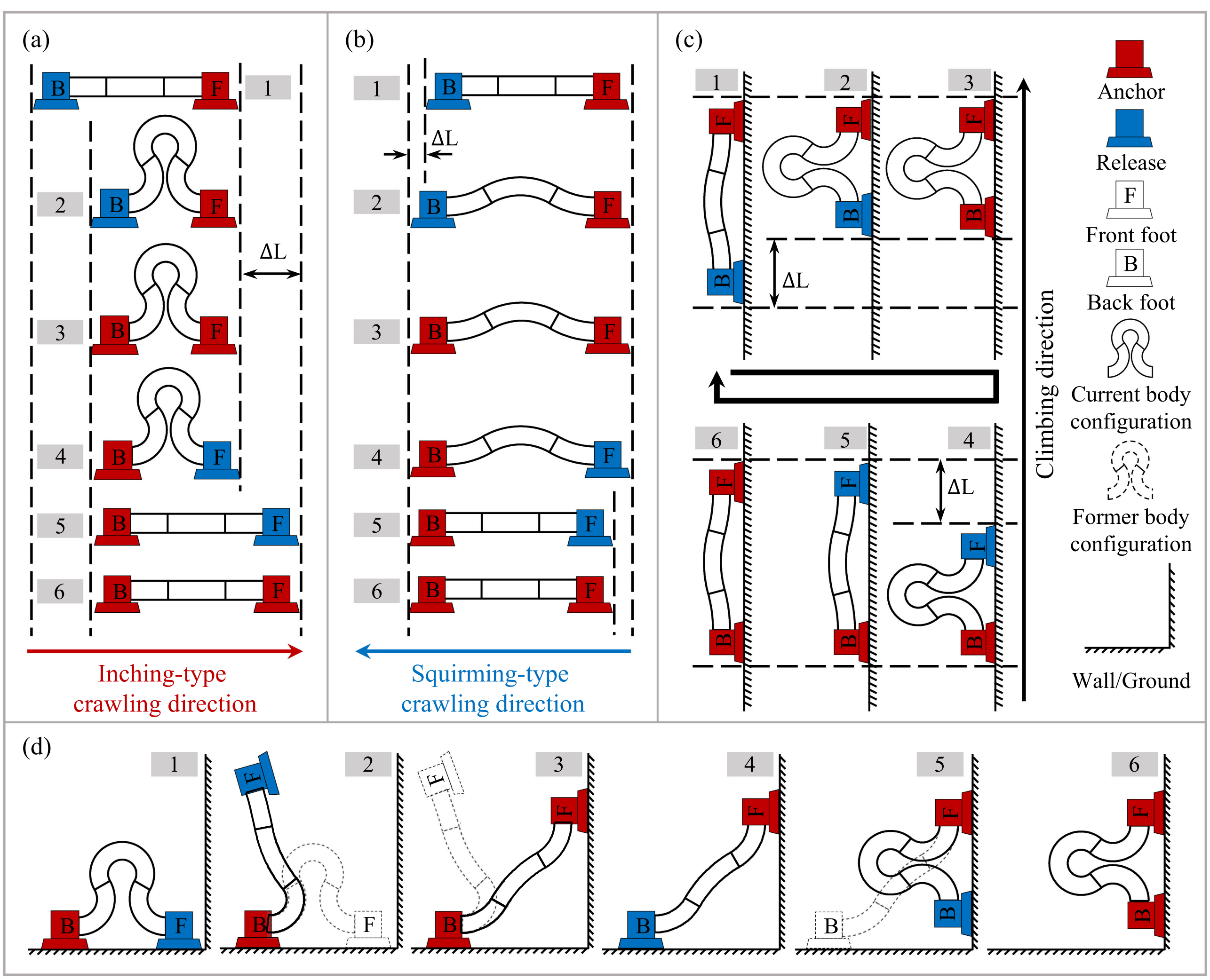

Fig. 7. Designed gaits sequence for different locomotion. The anchoring/releasing states of the suckers are represented by color red/blue. (a) Gait cycle designed for inching-type crawling locomotion. (b) Gait cycle designed for squirming-type crawling locomotion. (c) Gait cycle designed for climbing locomotion. (d) Gaits designed for initiative transitioning between crawling and climbing locomotion.

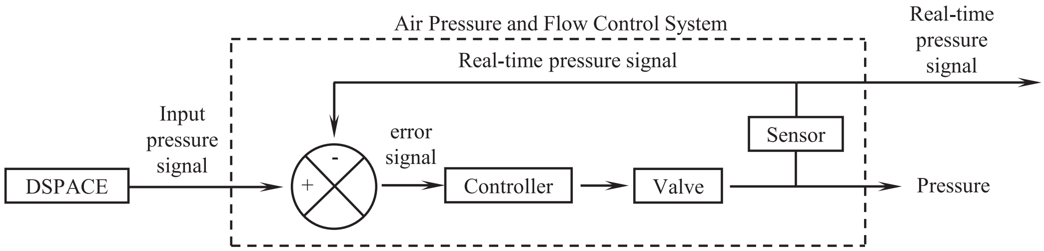

Fig. 8. Block diagram for five-channel air pressure and flow control system. The system is composed of the dSPACE analog signal input, controller, valves, and sensors.

the pitch of 2.5 mm. The reinforce fibers are wound along the superficial grooves with width and depth of 0.5 mm. Fibers are arranged in parallel with each other on three free surfaces of the air chamber to minimize the axial restraint of PAM deformation.

4) Connecting PAMs and Suckers: We connect all three PAMs in series and attach two sucker adhesive pads (SP-30, Kunshan Quanlifa Robot Technology Co., Ltd.) to the ends with 3D printed connectors. The robot is then connected to the pressure control system through five pneumatic channels (three for PAMs and two for sucker feet).

B. Pressure Control System

In multimodal locomotion experiments, we control the PAM deformation sequences and the anchoring status of suckers in different stages via the multichannel air pressure and flow control system (Fig. 8). Oil-free air compressor OTS750W-30 L (Outstanding Co., Ltd. Taizhou, China) is adopted as the input air source, which can provide a maximum pressure of 700 kPa with a flowing rate of 60 L/min. The dSPACE (MicroLab Box, dSPACE) is utilized to send analog input pressure signals to the pressure control system. Real-time pressure signals in different channels are obtained by the integrated sensors and sent to the dSPACE. The error signal is then transmitted to the controller to export control signals and control air pressure in the channel.

IV. Experimental Results

We conduct a series of experiments to demonstrate the multimodal locomotion capabilities including crawling, climbing, and transitioning in both air and aquatic environments. The SCCR can accomplish these locomotion mainly depending on the multi-DOF deformation of the robot body and the strong anchoring forces of sucker feet.

For each locomotion, we initially calculate the corresponding input quasi-static pressure sequences for the PAMs based on the analytical model and the desired motion gaits. The anchoring and releasing pressures of two sucker feet are also selected according to the experimental results is Fig. 4(b). Then the lasting time for different stages is tuned to leave enough time for the SCCR to deform between two quasi-static configurations and for the suckers to alternate the anchoring status. To simplify the control strategy, we regulate the sucker anchoring and releasing pressures at different suitable values. Based on the prior experimental results in Fig. 4(b), the sucker foot can provide an anchoring force larger than 6 N when the input negative pressure is greater than 20 kPa, which is enough to resist the body blocking forces in most cases according to Fig. 5(b). Thus, we set the sucker anchoring pressure at –20 kPa. The releasing pressure is selected to be 20 kPa to blow the sucker up from the ground, accelerating the releasing process.

A. Crawling

Different actuation pressure sequences are tested for inching-type and squirming-type locomotion. We observe from the crawling experimental results in Fig. 9(a) and (b) that the two types of crawling locomotion have opposite moving directions and different step lengths while controlled under the same feet anchoring sequence.

1) Inching-Type Crawling: For inching-type crawling [Fig. 9(a)], all three PAMs are totally deflated in stretched robot configuration in stages 1, 5, and 6. For stages 2, 3, and 4, the head, abdomen, and tail PAMs are bent at 120° (92 kPa), 240° (108 kPa), and 120° (92 kPa). The sucker anchoring/releasing pressure is –20/+20 kPa.

A cycle of inching-type crawling gaits takes no less than 2.5 s because it takes longer to depressurize the PAMs from higher pressure. The SCCR can inch at a maximum speed of 21 mm/s (0.11 body length/s) and dragging a payload of 500 g (about 15 times the self-weight, source and control units not included) on plastic horizontal planes. Although large deformation of PAMs results in dramatic motion of robot mass center, the sucker feet can easily form a seal cavity and provide enough anchoring force to fix steadily on planes, thanks to the contact force proposed by the self-weight.

2) Squirming-Type Crawling: For squirming-type crawling, the robot configuration is identical with that of inching-type in stages 1, 5, and 6. For the remaining stages 2, 3, and 4, the head, abdomen, and tail PAMs are bent at 35° (34 kPa), 70° (41 kPa), and 35° (34 kPa). The sucker anchoring/releasing pressure is also –20/+20 kPa. The five-channel monitored input pressures for squirming-type crawling is shown in Fig. 9(b). Squirming-type crawling locomotion can be adopted in application with confined environments and the actuation cycle period can be reduced to 0.65 s with a moving speed of 5 mm/s (0.026 body length/s).

B. Climbing

Compared with the crawling locomotion on planes, climbing on vertical walls is challenging due to the change of gravity direction (Fig. 10). The sucker contact surface turns vertically

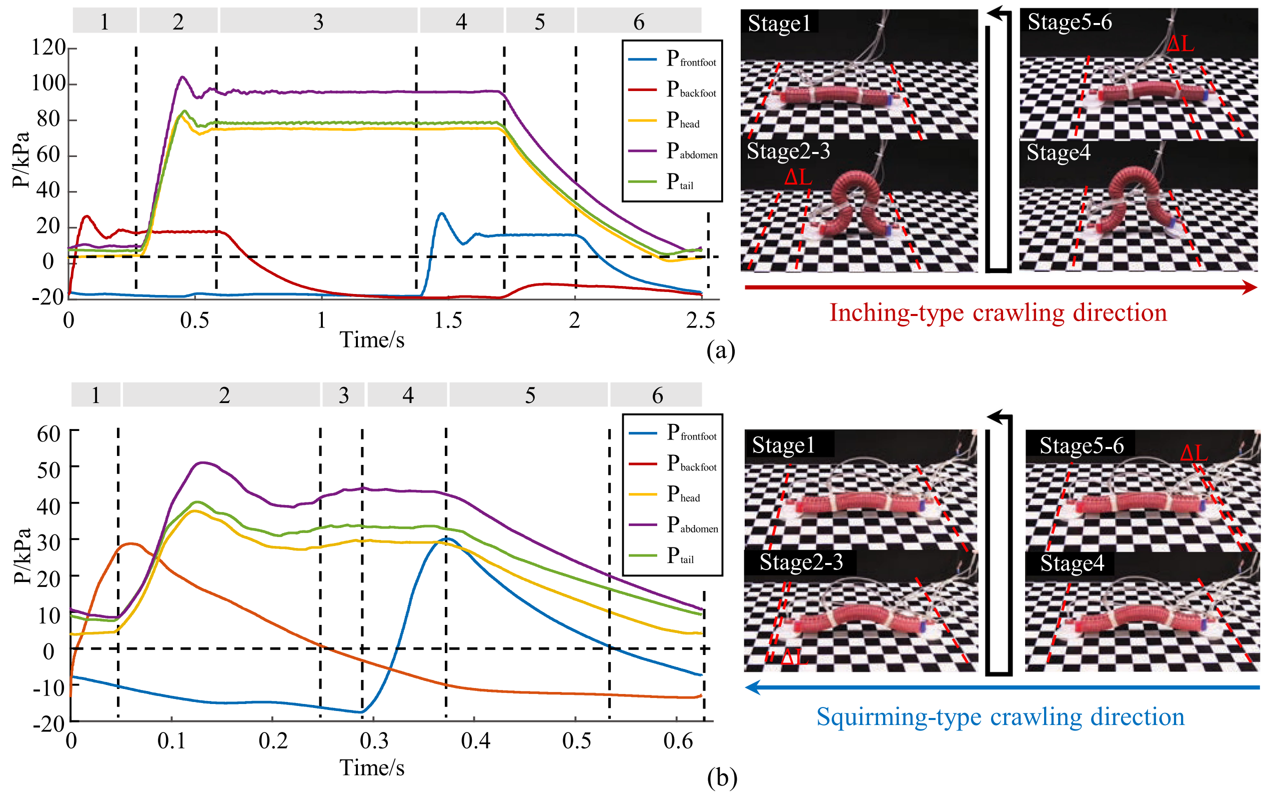

Fig. 9. Experimental results of the crawling locomotion. (a) Monitored five-channel input pressure in inching-type crawling locomotion. The actuation frequency is 0.4 Hz. The SCCR crawls with large arching height and large step length. (b) Monitored five-channel input pressure in squirming-type crawling locomotion. The actuation frequency is 1.54 Hz. The SCCR crawls with small arching height and step length.

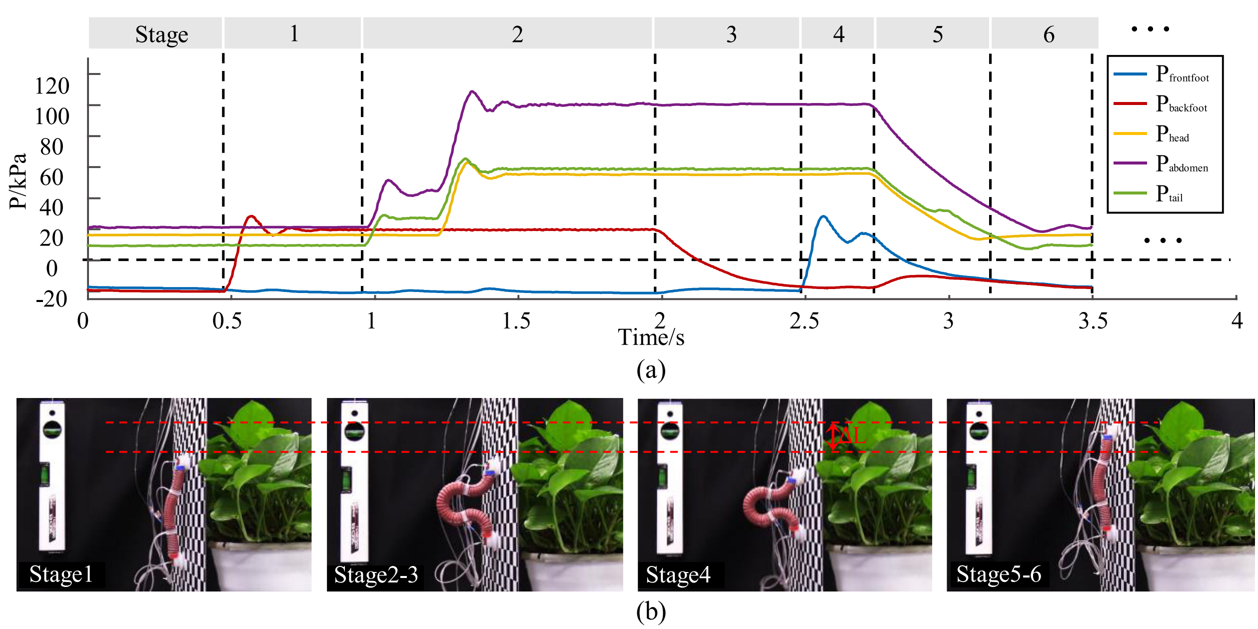

Fig. 10. Experimental results of the climbing locomotion. (a) Monitored five-channel input pressure of PAMs and suckers in climbing locomotion. (b) SCCR's gait sequence and step length in climbing locomotion on a vertical wall.

and the needed precontact force can no longer be provided by self-weight of the robot. On the contrary, the gravity force tends to peel the robot off from the wall due to the off-wall center of mass and results in noncompensable deformation of the PAMs, which may terminate the locomotion. When the robot is fully stretched and only the back foot is anchored, the front part of the robot tends to lean to the left or right side under minor interrupt. With cooperated deformation of three PAMs, we achieve an overall controllable robust climbing locomotion.

We implement a strategy in climbing and transitioning locomotion to revise the calculated input pressure of different PAMs accordingly so that the sucker precontact force can be provided by the body deformation when moving on walls. In the "Ω" deformation of the SCCR, the abdomen PAM plays the role of pushing the two ends of the robot body against the wall or the ground. On the other hand, the head or tail PAM plays the role of peeling the robot ends away from the locomotion plane. Thus, to counter the unfavorable peeling effect of the gravity and produce the precontact forces for sucker feet, the abdomen PAM pressure is tuned up and the head or tail PAM pressure is tuned down by ΔP in some configurations. As shown in Fig. 11, the designed gait sequence proposes a constraint of PAMs bending angles, which is plotted in solid line. The dotted shapes represent the adjusted body configuration if no wall is presented after the input pressures are revised. For example, in stage 4 of the climbing [Fig. 11(b)], the bending angles of three PAMs follow the constraint: $\phi = \alpha_1 - \alpha_2 + \alpha_3 = 0$. If we increase the original calculated input pressure of abdomen PAM by ΔP, the front suck foot would be pressed against the wall. Taking advantages of the compliance of PAMs, the SCCR can barely keep the same configuration as the solid line but also apply the precontact force to the sucker.

We can also use the similar strategy to obtain higher PAM stiffness to confront the peeling effect of gravity. For some configurations, the PAMs are not completely deflated to maintain the stiffness of PAMs. For example, in stage 5 of climbing locomotion shown in Fig. 11(c), we design the bending angles of PAMs to be positive rather than zero, while all the three bending angles still follow the original constraints of $\phi = \alpha_1 - \alpha_2 + \alpha_3 = 0$. The PAM stiffness is promoted while the body length barely changes.

Remark 1: In the climbing locomotion, many factors, e.g., robot configuration, gravity force direction, influence of payload, etc., could influence the gaits of SCCRs. The value of ΔP in this work is calibrated depending on the performance of SCCRs in several posture adjustments experiments. The theoretical value of ΔP can be determined by accurate modeling of robot deformation with external forces, which will be investigated in our future work by introducing bending sensors and designing a closed-loop controller.

In climbing locomotion experiments shown in Fig. 10, the head, abdomen, and tail PAMs are bent at 75° (60 kPa), 150° (100 kPa), and 75° (60 kPa), respectively, in stages 2, 3, and 4. For the remaining stages 1, 5, and 6, the three PAMs are partly deflated to 15° (17 kPa), 30° (21 kPa), and 15° (10 kPa), respectively. We set the anchoring/releasing pressure for sucker to be –20/+20 kPa and the actuation cycle period is extended

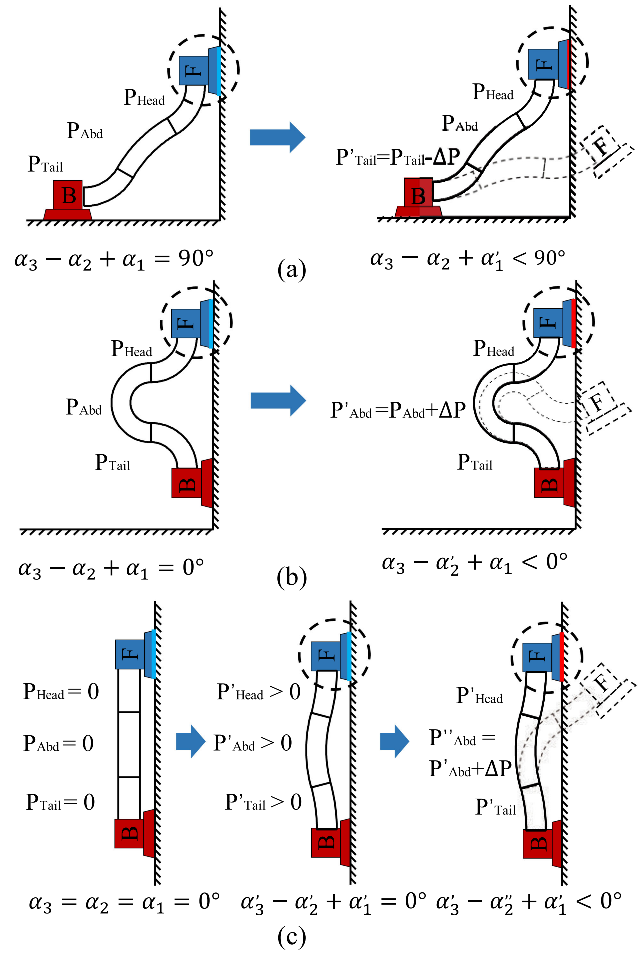

Fig. 11. Revision of input pressure of PAMs to obtain front sucker foot precontact forces and body stiffness in configurations of (a) stage 3 of transitioning locomotion; (b) stage 4 of climbing locomotion; (c) stage 5 of climbing locomotion. The dotted shapes represent the robot's theoretical configuration under the revised input pressure without boundary constraints of the wall.

to 3.5 s compared with the inching-type crawling locomotion. According to the experiments, the SCCR can climb upward and downward with a maximum speed of 15 mm/s (0.079 body length/s) on vertical walls.

C. Transitioning

The multi-DOF design of SCCR not only helps accomplish the climbing locomotion but also makes the transition from horizontal planes to vertical walls possible. Transitioning locomotion begins when SCCR crawls toward the wall and the front foot moves close enough to the corner.

The monitored input pressures and experiment results are plotted in Fig. 12 . In stage 1, the SCCR contracts into an "Ω" shape to drag the back foot toward its front end. The SCCR's configuration in stage 2 represents the head lifting process, similar to what an inchworm will do when it encounters a branch intersection or obstacle. In this progress, the tail PAM is bent to 136° (90 kPa) to lift the front part of SCCR up after the front foot is released in the previous stage. Then the abdomen and head PAMs are deflated to 28° (20 kPa) and 4° (5 kPa),

This article has been accepted for inclusion in a future issue of this journal. Content is final as presented, with the exception of pagination.

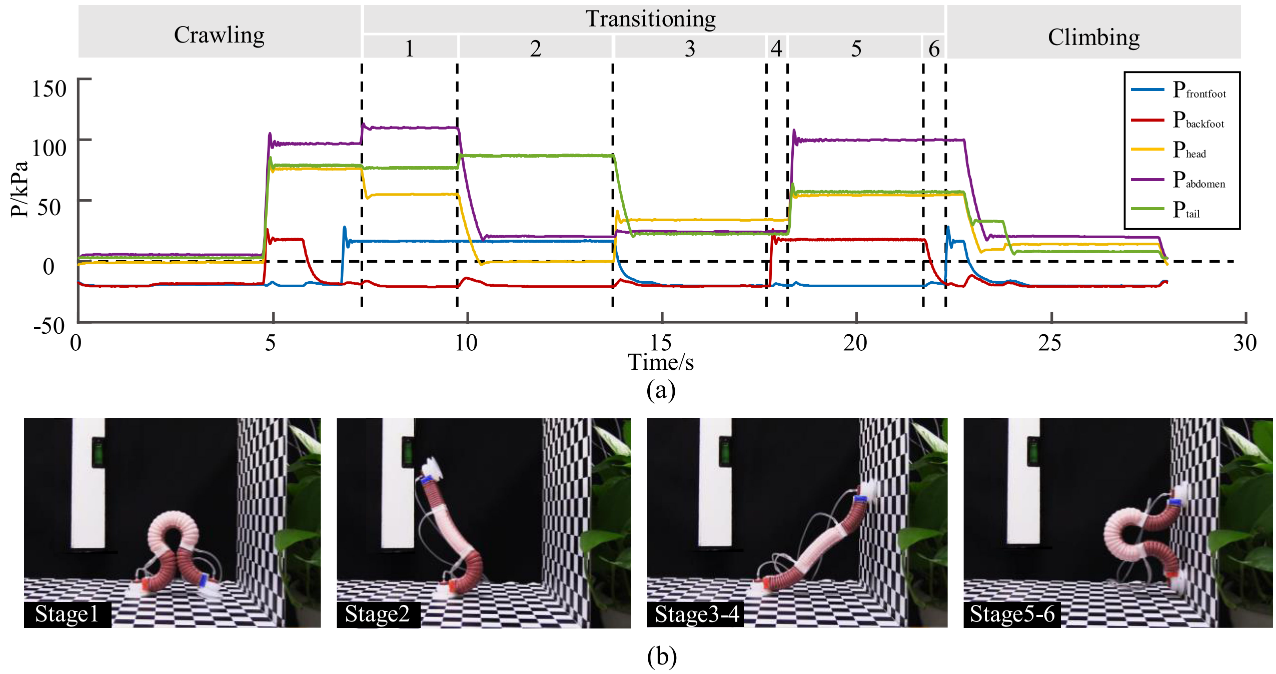

Fig. 12. Experimental results of the transitioning locomotion. (a) Monitored five-channel input pressure of PAMs and suckers in transitioning locomotion. (b) SCCR's gait sequence from crawling on the ground to climbing on the vertical wall.

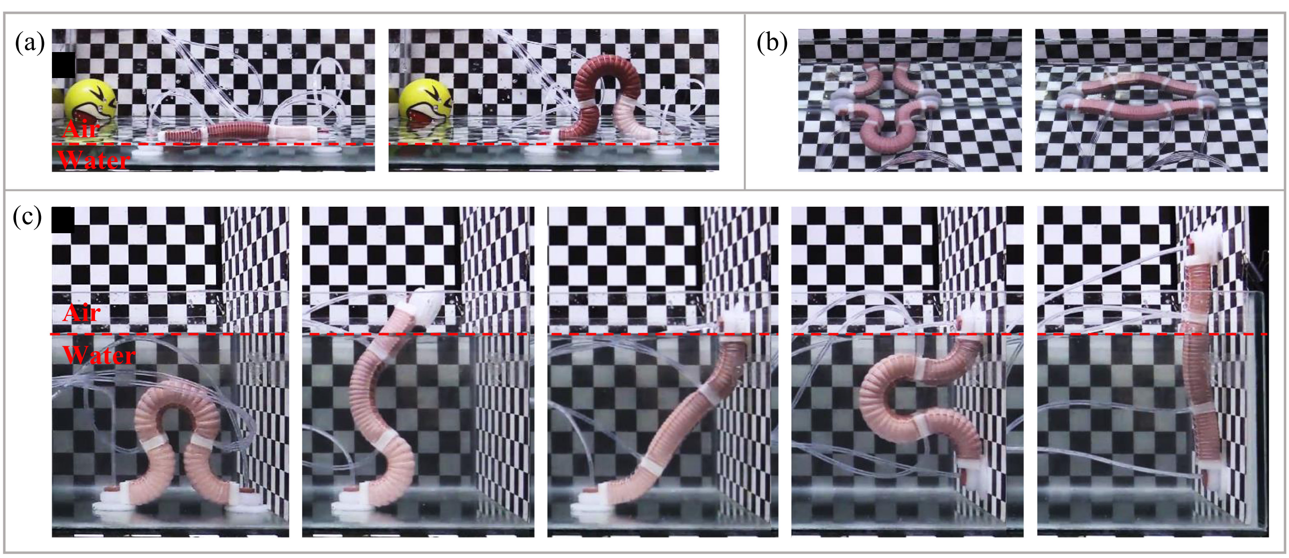

Fig. 13. Different locomotion of SCCRs in aquatic environments. (a) Crawling in shallow water (1.5 cm in depth, 0.5 robot body height). (b) Crawling on the tank side wall in water (12 cm in depth, 4 robot body height). The SCCR is totally submerged. (c) Locomotion transitioning from crawling to climbing in water (12 cm in depth, 4 robot body height). Part of the locomotion is performed in the half-water half-air environment.

respectively, to stretch the front robot body out. To finish the "wall fitting" process in stage 3, the vacuum pump connected to the front sucker is first turned on and the tail PAM is then partly deflated to 60° (25 kPa) to press the front foot onto the wall, while the head and abdomen PAMs are bent to 60° (40 kPa) and 30° (25 kPa). In this case, the back foot is anchored on the plane and the front foot is anchored on the wall, and the body deforms to fit in the corner space and bridge between two feet. In the following stages 4, 5, and 6, the back foot is first released and the SCCR contracts into an "Ω" shape again with head, abdomen, and tail PAMs inflated to 75° (60 kPa), 150° (100 kPa), and 75° (60 kPa), respectively, to pull the back foot onto the wall. After the back foot is anchored, the SCCR can continue to climb on the vertical wall. The sucker anchoring/releasing pressure is set to be –20/+20 kPa and the observed small pressure disturbance around –20 kPa in Fig. 12(a) represents the leak caused by motion of the SCCR.

Remark 2: The abdomen PAM we adopt for transitioning locomotion in Fig. 12(b) appears whitish pink, which is different from the remaining PAMs. It is because the red pigment in silicone gel Elastosil M4601 Part A (Wacker Chemie AG, Germany) deposits before usage. The color of the PAM has no impact on the material's mechanical properties.

D. Locomotion in Aquatic Environments

Most of the locomotion presented above can be replicated in aquatic environments if the SCCR is hydraulically actuated. The density of the used material ranges from 1.1 to 1.5 g/mm^3; thus, we need to replace the air pumped into the chamber with water to prevent the robot from floating in water.

It is demonstrated that the SCCR is capable of crawling in shallow water (1.5 cm in depth, 0.5 robot body height) where the sucker adhesive surfaces are submerged in the water and most of the SCCR body arches out of the water; thus, the buoyancy is negligible [Fig. 13(a)]. In this case, the SCCR can be actuated with water or air and the locomotion gaits are identical with those of crawling on the ground.

The SCCR can also crawl horizontally on the side wall of the tank in water [Fig. 13(b)], which is difficult to achieve on the ground. The average density of the SCCR is slightly larger than the water if the PAMs are filled with water. With the whole robot submerged in water, most of the robot self-weight is confronted by buoyancy and the suspended robot parts is kept from falling down when one of the suckers is released.

Finally, we demonstrate in Fig. 13(c) that the SCCR can accomplish transitioning locomotion in water (12 cm in depth, 4 robot body height). The SCCR first performs one step of crawling locomotion in aquatic environments, and then the SCCR conducts transitioning and one-step climbing locomotion in half-water half-air environment. The body configuration and actuation sequence in this case are analogous with those designed for on-ground locomotion. The results illustrate that the PAM deformation and sucker adhesive principles are applicable for both terrestrial and aquatic environments. The SCCR can easily break through the boundary between two environments.

V. Conclusion

In summary, this work presented an inchworm-inspired multimodal SCCR that is capable of crawling on horizontal planes, climbing on vertical walls, and initiative transitioning between them. The SCCR is composed of three bending PAMs, which are designed to produce "Ω" deformation, and two negative pressure suckers, which can provide controllable friction forces. Also, a simplified kinematic model was developed to characterize the kinematic features of the SCCR. A five-channel air pressure control system was adopted to accomplish real-time precise pressure control and sensing. Different locomotion gaits, including two types of crawling, climbing, and transitioning, were designed and verified. The locomotion experiments illustrated that the SCCR crawls at the highest speed of 21 mm/s (0.11 body length/s) and climbs at the highest speed of 15 mm/s (0.079 body length/s). The SCCR is also capable of dragging a payload up to 500 g (about 15 times the self-weight) on plastic surfaces, and moving in aquatic environments, which shows great potential of accomplishing tasks like maintenance, detection, surveillance, and manipulation in various unstructured environments.

Therefore, the distinct feature of this article is that we designed a PAM-based SCCR which can solve the locomotion transitioning challenges encountered in previous crawling–climbing robot designs by imitating the gaits observed in biological inchworms. To the best of our knowledge, there is no reported soft robot that can achieve such multimodal locomotion, especially the transition between crawling and climbing locomotion. In the future, we will try to develop an analytical model for PAM deformation with constraints and external forces. Also, possibilities of SCCR locomotion on planes with incline angles ranging from 90° to 180° can be explored. Further, additional sensors (such as shape sensors for PAMs, contact force sensors for feet, etc.) can be implemented into the system to predict the success or failure of the multimodal locomotion and develop a feedback controller for the posture adjustment of the SCCR.

References

[1] M. Minor, H. Dulimarta, G. Danghi, R. Mukherjee, R. L. Tummala, and D. Aslam, "Design, implementation, and evaluation of an under-actuated miniature biped climbing robot," in *Proc. IEEE/RSJ Int. Conf. Intell. Robots Syst. (Cat. No. 00CH37113)*, vol. 3, 2000, pp. 1999–2005.

[2] Y. Guan *et al.*, "A modular biped wall-climbing robot with high mobility and manipulating function," *IEEE/ASME Trans. Mechatronics*, vol. 18, no. 6, pp. 1787–1798, Dec. 2013.

[3] M. P. Murphy and M. Sitti, "Waalbot: An agile small-scale wall-climbing robot utilizing dry elastomer adhesives," *IEEE/ASME Trans. Mechatronics*, vol. 12, no. 3, pp. 330–338, Jun. 2007.

[4] O. Unver and M. Sitti, "Tankbot: A palm-size, tank-like climbing robot using soft elastomer adhesive treads," *Int. J. Robot. Res.*, vol. 29, no. 14, pp. 1761–1777, 2010.

[5] T. Seo and M. Sitti, "Under-actuated tank-like climbing robot with various transitioning capabilities," in *Proc. IEEE Int. Conf. Robot. Autom.*, 2011, pp. 777–782.

[6] G. Lee, H. Kim, K. Seo, J. Kim, and H. S. Kim, "Multitrack: A multi-linked track robot with suction adhesion for climbing and transition," *Robot. Auton. Syst.*, vol. 72, pp. 207–216, 2015.

[7] G. Alici, T. Canty, R. Mutlu, W. Hu, and V. Sencadas, "Modeling and experimental evaluation of bending behavior of soft pneumatic actuators made of discrete actuation chambers," *Soft Robot.*, vol. 5, no. 1, pp. 24–35, 2018.

[8] K. Elgeneidy, N. Lohse, and M. Jackson, "Bending angle prediction and control of soft pneumatic actuators with embedded flex sensors-a data-driven approach," *Mechatronics*, vol. 50, pp. 234–247, 2018.

[9] C. Christianson, N. N. Goldberg, D. D. Deheyn, S. Cai, and M. T. Tolley, "Translucent soft robots driven by frameless fluid electrode dielectric elastomer actuators," *Sci. Robot.*, vol. 3, no. 17, 2018, Art no. eaat 1893.

[10] X. Ji *et al.*, "An autonomous untethered fast soft robotic insect driven by low-voltage dielectric elastomer actuators," *Sci. Robot.*, vol. 4, no. 37, 2019, Art no. eaaz 6451.

[11] H. Jin, Y. Ouyang, H. Chen, J. Kong, W. Li, and S. Zhang, "Modeling and motion control of a soft SMA planar actuator," *IEEE/ASME Trans. Mechatronics*, to be published. doi: 10.1109/TMECH.2021.3074971.

[12] J. Koh and K. Cho, "Omega-shaped inchworm-inspired crawling robot with large-index-and-pitch (LIP) SMA spring actuators," *IEEE/ASME Trans. Mechatronics*, vol. 18, no. 2, pp. 419–429, Apr. 2013.

[13] B. Jin, H. Song, R. Jiang, J. Song, Q. Zhao, and T. Xie, "Programming a crystalline shape memory polymer network with thermo-and photo-reversible bonds toward a single-component soft robot," *Sci. Adv.*, vol. 4, no. 1, 2018, Art no. eaao 3865.

[14] D. Rus and M. T. Tolley, "Design, fabrication and control of soft robots," *Nature*, vol. 521, no. 7553, pp. 467–475, 2015.

[15] G. Gu, J. Zhu, L. Zhu, and X. Zhu, "A survey on dielectric elastomer actuators for soft robots," *Bioinspiration Biomimetics*, vol. 12, no. 1, 2017, Art no. 0 11003.

[16] S. Coyle, C. Majidi, P. LeDuc, and K. J. Hsia, "Bio-inspired soft robotics: Material selection, actuation, and design," *Extreme Mechanics Lett.*, vol. 22, pp. 51–59, 2018.

[17] C. Majidi, "Soft robotics: A perspective-current trends and prospects for the future," *Soft Robot.*, vol. 1, no. 1, pp. 5–11, 2014.

[18] S. Kim, C. Laschi, and B. Trimmer, "Soft robotics: A bioinspired evolution in robotics," *Trends Biotechnol.*, vol. 31, no. 5, pp. 287–294, 2013.

[19] Y. Sugiyama and S. Hirai, "Crawling and jumping of deformable soft robot," in *Proc. IEEE/RSJ Int. Conf. Intell. Robots Syst. (IEEE Cat. No 04CH37566)*, vol. 4, 2004, pp. 3276–3281.

[20] W. Wang, H. Zhang, and J. Zhang, "Crawling locomotion of modular climbing caterpillar robot with changing kinematic chain," in *Proc. IEEE/RSJ Int. Conf. Intell. Robots Syst.*, 2009, pp. 5021–5026.

[21] H. Guo, J. Zhang, T. Wang, Y. Li, J. Hong, and Y. Li, "Design and control of an inchworm-inspired soft robot with omega-arching locomotion," in *Proc. IEEE Int. Conf. Robot. Autom.*, 2017, pp. 4154–4159.

[22] A. Rafsanjani, Y. Zhang, B. Liu, S. M. Rubinstein, and K. Bertoldi, "Kirigami skins make a simple soft actuator crawl," *Sci. Robot.*, vol. 3, no. 15, 2018, Art no. eaar 7555.

[23] Z. G. Joey, A. A. Calderón, and N. O.Pérez-Arancibia, "An earthworm-inspired soft crawling robot controlled by friction," in *Proc. IEEE Int. Conf. Robot. Biomimetics*, 2017, pp. 834–841.

[24] E. B. Joyee and Y. Pan, "A fully three-dimensional printed inchworm-inspired soft robot with magnetic actuation," *Soft Robot.*, vol. 6, no. 3, pp. 333–345, 2019.

[25] H. Wang and A. Yamamoto, "Analyses and solutions for the buckling of thin and flexible electrostatic inchworm climbing robots," *IEEE Trans. Robot.*, vol. 33, no. 4, pp. 889–900, Aug. 2017.

[26] Y. Wu *et al.*, "Insect-scale fast moving and ultrarobust soft robot," *Sci. Robot.*, vol. 4, no. 32, 2019, Art no. eaax 1594.

[27] S. Rozen-Levy, W. Messner, and B. A. Trimmer, "The design and development of branch bot: A branch-crawling, caterpillar-inspired, soft robot," *Int. J. Robot. Res.*, vol. 40, no. 1, pp. 24–36, 2021.

[28] G. Singh and G. Krishnan, "Designing fiber-reinforced soft actuators for planar curvilinear shape matching," *Soft Robot.*, vol. 7, no. 1, pp. 109–121, 2020.

[29] G. Gu, J. Zou, R. Zhao, X. Zhao, and X. Zhu, "Soft wall-climbing robots," *Sci. Robot.*, vol. 3, no. 25, 2018, Art no. eaat 2874.

[30] B. Liao *et al.*, "Soft rod-climbing robot inspired by winding locomotion of snake," *Soft Robot.*, vol. 7, no. 4, pp. 500–511, 2020.

[31] D. Xie, J. Liu, R. Kang, and S. Zuo, "Fully 3D-printed modular pipe-climbing robot," *IEEE Robot. Autom. Lett.*, vol. 6, no. 2, pp. 462–469, Apr. 2021.

[32] Y. Zhang, L. Ge, J. Zou, H. Xu, and G. Gu, "A multimodal soft crawling-climbing robot with the controllable horizontal plane to slope transition," in *Proc. IEEE/RSJ Int. Conf. Intell. Robots Syst.*, 2019, pp. 3343–3348.

[33] L. Van Griethuijsen and B. Trimmer, "Locomotion in caterpillars," *Biol. Rev.*, vol. 89, no. 3, pp. 656–670, 2014.

[34] B. Trimmer and J. Issberner, "Kinematics of soft-bodied, legged locomotion in manduca sexta larvae," *Biol. Bull.*, vol. 212, no. 2, pp. 130–142, 2007.

[35] J. Brackenbury, "Fast locomotion in caterpillars," *J. Insect Physiol.*, vol. 45, no. 6, pp. 525–533, 1999.

[36] P. Polygerinos *et al.*, "Modeling of soft fiber-reinforced bending actuators," *IEEE Trans. Robot.*, vol. 31, no. 3, pp. 778–789, Jun. 2015.

[37] F. Connolly, C. J. Walsh, and K. Bertoldi, "Automatic design of fiber-reinforced soft actuators for trajectory matching," *Proc. Nat. Acad. Sci.*, vol. 114, no. 1, pp. 51–56, 2017.

[38] Y. Hao *et al.*, "A multimodal, enveloping soft gripper: Shape conformation, bioinspired adhesion, and expansion-driven suction," *IEEE Trans. Robot.*, vol. 37, no. 2, pp. 350–362, Apr. 2021.

[39] L. R. Herrmann, "Elasticity equations for incompressible and nearly incompressible materials by a variational theorem." *AIAA J.*, vol. 3, no. 10, pp. 1896–1900, 1965.

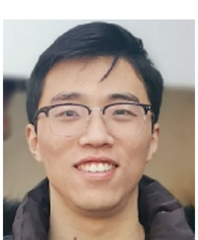

Yifan Zhang received the B.E. degree (Hons.) in mechanical engineering from Shanghai Jiao Tong University, Shanghai, China, in 2020.

He is currently a Research Assistant with Soft Robotics and Biodesign Lab, Shanghai Jiao Tong University. His research interests include mechatronics, soft pneumatic actuator design, and soft robot locomotion control.

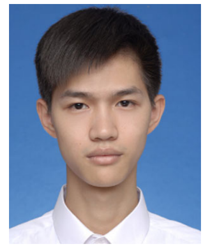

Dezhi Yang received the B.E. degree in mechanical engineering in 2020 from Shanghai Jiao Tong University, Shanghai, China, where he is currently working toward the M.S. degree in mechanical engineering.

His research interests include design and control of bioinspired soft robots, and soft wearable systems for assistance and rehabilitation.

Peinan Yan received the B.E. degree in mechanical engineering in 2020 from Shanghai Jiao Tong University, Shanghai, China, where he is currently working toward the M.S. degree in mechanical engineering.

His research interests include design and control of dielectric elastomer actuators.

Peiwei Zhou received the B.E. degree in mechanical engineering in 2020 from Shanghai Jiao Tong University, Shanghai, China, where he is currently working toward the M.S. degree in mechanical engineering.

His research interests include design and control of bioinspired soft robot, soft biomimetic hand for prosthesis usage, and industrial grasping.

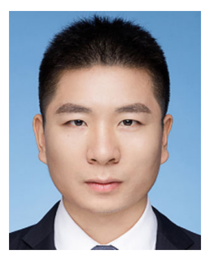

Jiang Zou received the Ph.D. degree (Hons.) in mechatronic engineering from Shanghai Jiao Tong University, Shanghai, China, in 2019.

Being supported by Shanghai Postdoctoral Excellence Program, he is a Postdoctor with Shanghai Jiao Tong University. His research interests include design, modeling, and control of soft robots.

Guoying Gu (Senior Member, IEEE) received the B.E. degree (Hons.) in electronic science and technology and the Ph.D. degree (Hons.) in mechatronic engineering from Shanghai Jiao Tong University, Shanghai, China, in 2006 and 2012, respectively.

Since 2012, he has been with Shanghai Jiao Tong University, where he is currently appointed as a Professor with School of Mechanical Engineering. He was a Humboldt Fellow with University of Oldenburg, Oldenburg, Germany. He was a Visiting Scholar with Massachusetts Institute of Technology, Cambridge, MA, USA; National University of Singapore, Singapore; and Concordia University, Montreal, QC, Canada. His research interests include soft robotics, bioinspired and wearable robots, smart materials sensing, actuation, and motion control. He is the author or coauthor of more than 100 publications, which have appeared in *Nature Biomedical Engineering*, *Science Robotics*, *Science Advances*, *Advanced Materials*, *National Science Review*, *IEEE/ASME Transactions*, *Advanced Functional Materials*, *Soft Robotics*, etc., as book chapters and in conference proceedings.

Dr. Gu is the Recipient of the National Science Fund for Distinguished Young Scholars. He currently serves as an Associate Editor for IEEE TRANSACTIONS ON ROBOTICS and *IEEE Robotics and Automation Letters*. He has also served for several journals as Editorial Board Member, Topic Editor, or Guest Editor, and several international conferences/symposiums as Chair, Co-Chair, Associate Editor, or Program Committee Member.